Contents lists available at ScienceDirect

Arabian Journal of Chemistry

journal homepage: www.ksu.edu.sa

Pyroelectric field drived photocatalysis by $ZnFe_2O_4/NaNbO_3$ heterojunction for dye degradation through integration of solar and thermal energy

Di Zhou [a,1], Xiaoju Zhou [b,1], Zhenglong Hu [b,*], Lili Zheng [a], Yu Tian [a], Yafang Tu [a], Chunbo Hua [b], Li Xue [b], Juan Xiong [c,*]

[a] School of Optoelectronic Materials and Technology, Jianghan University, Wuhan 430056, PR China
[b] School of Electronic and Information Engineering, Key Laboratory of Optoelectronic Sensing and Intelligent Control, Hubei University of Science and Technology, Xianning 437100, PR China
[c] Hubei Key Laboratory of Micro-nanoelectronic Materials and Devices, School of Microelectronics, Hubei University, Wuhan 430062, PR China

ARTICLE INFO

Keywords:
Sodium niobate ($NaNbO_3$)
Zinc ferrite ($ZnFe_2O_4$)
Heterojunction
Pyroelectric effect
Photocatalysis

ABSTRACT

A novel composite of $ZnFe_2O_4/NaNbO_3$ (ZFO/NNO) nanorods with a p-n heterojunction structure was successfully synthesized via the hydrothermal method. The NNO nanorods were heated in situ using the photothermal effect of ZFO and subsequently cooled to room temperature, creating a cyclic heating and cooling process for ZFO/NNO. The catalytic activity of the resulting nanorods was assessed through the degradation of Rhodamine B, reaching 98% degradation efficiency after 180 min, attributed to the synergistic effect of pyrocatalysis and photocatalysis. Compared with NNO and ZFO individually, the enhanced performance of ZFO/NNO can be attributed to several synergistic factors, including the expanded spectral range of light absorption for ZFO, the establishment of the built-in electric field of the p-n junction between ZFO and NNO, and the NNO pyroelectric effect that further improved the charge transfer efficiency. Superoxide radicals and holes generated from photo-induced electrons were identified as the active species. Hydroxyl radicals generated from pyroelectrically-induced charge also participated in catalytic reaction. The combined effect of pyroelectric and photocatalytic processes could significantly improve the coupled pyro-photocatalytic reaction for pyroelectric semiconductor heterostructure, enabling the utilization of multiple energy sources, including solar and thermal energy.

1. Introduction

Photocatalytic technology is a widely recognized and significant approach for utilizing solar energy and has the potential to alleviate global environmental pollution and energy crises (Tu et al., 2020; Dai et al., 2023; Li et al., 2021). Significant advances have been made in the field of photocatalysis since the seminal paper reported by Fujishima and Honda in 1972. However, the practical application of photocatalytic degradation of contaminants still faces major challenges due to the high recombination rate of electron-hole pairs and low sunlight utilization efficiency. Natural diurnal temperature fluctuations, in addition to solar energy, also offer an inexhaustible energy resource (Ou et al., 2016; Wu et al., 2020; Jiang et al., 2021). Developing a new and environmentally friendly catalytic technology that utilizes diurnal temperature variations to treat dye wastewater is crucial.

Certain materials exhibit a property known as the pyroelectric effect. This effect describes the variation in spontaneous polarization that these materials undergo in response to temperature changes between hot and cold states (Jiang et al., 2021; Chen et al., 2019; Zhang et al., 2021). Temperature fluctuations and mechanical vibrations induce ion displacement as the dipole moment changes within pyroelectric and piezoelectric materials. This creates a net electric charge and an electric potential on the material's surface. The intrinsic electric field can effectively address rapid carrier recombination in the bulk phase (Liu et al., 2022; Li et al., 2014). Additionally, pyroelectric-induced surface charge generate reactive oxygen species (ROS), including hydroxyl radicals (·OH), superoxide radicals ($\cdot O_2^-$), singlet oxygen ($^1O_2$), and hydrogen peroxide (H_2O_2) (Benke et al., 2015; Wu et al., 2016; Huang

* Corresponding authors.
E-mail addresses: huzhenglong@hbust.edu.cn (Z. Hu), juanxiong@hubu.edu.cn (J. Xiong).
[1] These authors contributed equally to this work.

https://doi.org/10.1016/j.arabjc.2024.105996
Received 9 June 2024; Accepted 17 September 2024
Available online 18 September 2024

et al., 2022). Pyro-catalytically generated ROS are widely thought to have huge potential for disinfection and treatment of dyes (Raufeisen et al., 2020). Qian et al. combined the pyroelectric effect with electrochemical oxidation using ZnO nanorods and reported a thermocatalytic process with a decomposition rate of approximately 98.15 % for Rhodamine B (RhB) solution under 22–62 °C heating–cooling cycles (Qian et al., 2017). Jia et al. reported the pyro-catalytic activity of pyroelectric $BiFeO_3$ nanoparticles for dye degradation under thermal cycles of 27–38 °C (Wu et al., 2016). Liu et al. reported on the enhanced pyro-photo-electric performance of $Ba_{1-x}Sr_xTiO_3$ catalyst attributed to the acceleration of carrier separation and transfer efficiency due to the built-in polarization electric field present in pyroelectric materials (Liu et al., 2022).

Sodium niobate ($NaNbO_3$, NNO), a perovskite material with semiconductor properties, has attracted considerable research interest due to its excellent nonlinear optics, ferroelectricity, ionic conductivity, and photo-refractive properties. Moreover, NNO exhibits excellent pyroelectric properties, including a large pyroelectric coefficient of about 100 $\mu C \bullet m^{-2} \bullet K^{-1}$ and a high Curie temperature (370 °C) (Jung et al., 2011). These properties make it a promising choice for room-temperature pyroelectric catalytic processes (Guo et al., 2023; Zhang et al., 2019). Zhang et al. demonstrated the effectiveness of combining pyroelectric catalysis and photoelectrochemical catalysis in an NNO-based system, proving the feasibility of pyroelectric-assisted photoelectrochemical performance (Zhang et al., 2021; Li et al., 2020; Zhang et al., 2021). You et al. documented the pyrocatalytic decomposition performance of NNO with different morphologies under a heating–cooling cycle of 23–50 °C (You et al., 2018). Liu et al. reported on an optimized NNO nanostructure and noted that the synergy between the optimized pyroelectric effect and surface reaction dynamics can enhance the dynamics of photo- and pyro-generated carrier transfer (Li et al., 2022). Liu et al. substantiated the synergistic effect of piezoelectric/pyroelectric-driven mechano/pyro bi-catalysis of NNO nanofibers (You et al., 2018). However, the wide band gap of NNO ($E_g \sim$ 3.3 eV) significantly limited its photoreaction in the solar spectral region, indicating that most solar energy was not utilized by the original NNO photocatalyst. Additionally, the currently available pyroelectric materials, whose pyrocatalytic capability depends on the variation of ambient temperature, exhibit low pyrocatalytic efficiencies. Under steady-state conditions, the short-circuit pyrocurrent (I) available for pyrocatalytic reactions can be calculated as (Wang et al., 2022; You et al., 2022):

$$I = p \cdot A \cdot dT/dt \quad (1)$$

where p is the pyroelectric coefficient, A is the area of the surface perpendicular to the polarization direction, and dT/dt is the temperature change rate. The maximum pyroelectric current available for the pyrocatalytic reaction is only about 1–5 $nA \cdot cm^{-2}$, which translates to two to three orders of magnitude lower than that of photocatalysts (Wang et al., 2019). This limitation arises because changing the ambient temperature to achieve a significant effect requires overcoming the huge heat capacity of the surrounding media, resulting in a slow rate of temperature change (dT/dt). Ideally, a localized heat source would be employed to heat only the pyrocatalytic material itself to a certain degree while keeping the ambient temperature almost unchanged.

Photothermal agent nanostructures, which absorb light and convert it into heat, are one such ideal candidate (Mateo et al., 2021; Yang et al., 2021). $ZnFe_2O_4$ (ZFO), a type of ferrite with a spinel structure, exhibits various functionalities, including soft magnetism, antibacterial properties, and photocatalysis, and is inexpensive, non-toxic, environmentally friendly, and highly chemically stable (Sun et al., 2024). Importantly, ZFO possesses a narrow band gap of about 1.9 eV, enabling efficient utilization of solar energy (Zhang et al., 2022). Recent studies have highlighted ZFO's potential as a superior photothermal agent, demonstrating a superior and stable ability to convert light into heat. For example, Yang et al. reported ZFO nanoparticles that exhibited a temperature increase of 36.8 °C and a photothermal conversion efficiency of 37.7 % under near-infrared light irradiation of 808 nm (Wang et al., 2019). Wang et al. investigated a composite structure of ZnO/ZFO and proposed that the photothermal effect of ZFO accelerated the migration of reactive oxygen species (ROS) and, consequently, the catalytic reaction rate (Zhang et al., 2023). Additionally, Han et al. documented the synthesis of ZFO with oxygen vacancies via a soft-chemistry method, demonstrating its high performance in the photothermal catalytic degradation of gaseous organic pollutants (Sun et al., 2021).

In addition to the utilization of solar and thermal energy, one-dimensional (1D) materials, such as nanowires, nanorods, and nanofibers, have attracted significant research interest for nanostructure design due to their high aspect ratio, quantum confinement effects, and a significantly higher density of active sites, which are expected to lead to substantially enhanced photocatalytic activities (Qian et al., 2017; You et al., 2018; Xiao et al., 2015; Antonin et al., 2024). Motivated by these considerations, this work investigates a photocatalyst synthesized through the hydrothermal method comprised of ZFO-decorated NNO nanorods. In this composite structure combining pyroelectric and photothermal materials, light irradiation heats the catalyst, while the surrounding environment cools it. This cyclic heating and cooling process removes the requirement for additional energy input. The study demonstrates that the photocatalyst temperature can be modulated from room temperature to 45 °C under simulated sunlight irradiation. The degradation efficiency of RhB reached 98 % under temperature variation and light irradiation, achieving a degradation rate that was two times higher than that of its photocatalysis-only counterpart and 2.8 times higher than that of pristine ZFO, respectively. This improvement in dye degradation was attributed to the synergistic combination of pyroelectric catalysis with photocatalysis. This research has the potential to introduce a new approach for synergistic pyroelectric catalysis and elucidate the joint enhancement mechanism of the pyroelectric effect and photocatalysis, thus offering promising applications for pollutant treatment.

2. Experimental section

2.1. Synthesis of materials

All chemicals used in this experiment were analytical grade reagents, purchased from Sinopharm Chemical Reagent Co. Ltd. (China), and employed without any further purification steps.

2.1.1. Synthesis of NNO

NNO nanorods (NNO NRs) were synthesized via hydrothermal reaction and subsequent annealing treatment, following a previously reported method (Li et al., 2020; Li et al., 2022). To prepare the solution, 0.57 g Nb_2O_5 powder was added to 40 mL of 10 M NaOH aqueous solution and stirred for 2 h. The resulting suspension was transferred into Teflon-lined stainless-steel autoclaves, and a hydrothermal reaction was conducted at 160 °C for 2 h. After the reaction, the autoclaves were removed and allowed to cool down under ambient conditions. The precipitate obtained after filtration was washed with deionized water and ethanol to achieve a neutral pH in the supernatant. Then, the precipitate was dried at 80 °C for 12 h. The resulting NNO NRs were obtained after being treated at 500 °C for 2 h. For comparison purposes, NNO microcubes (NNO MCs) were prepared by extending the hydrothermal reaction time to 8 h while keeping all other conditions unchanged (Yu et al., 2012).

2.1.2. Preparation of ZFO nanoparticles

ZFO nanoparticles were synthesized using a solvothermal method following a previously documented procedure (Xu et al., 2022). Briefly, 0.06 mmol of $Fe(NO_3)_3 \cdot 9H_2O$ was dissolved in a 30 mL solution of ethylene glycol/isopropyl alcohol (volume ratio: 5/3) under stirring at

room temperature. Subsequently, 0.03 mmol of $Zn(CH_3COO)_2{\cdot}2H_2O$ was added and stirred until complete dissolution. The mixture was then transferred to a 50 mL Teflon-lined autoclave and heated at 180℃ for 12 h. After cooling naturally to room temperature, the product was isolated by centrifugation, washed three times with purified water and once with anhydrous ethanol, and finally dried at 80℃ for 10 h.

2.1.3. Preparation of ZFO/NNO composites

NNO/ZFO composites were prepared by a sequential hydrothermal-solvothermal method. The NNO NRs/MCs prepared via the aforementioned hydrothermal method were added to a reactor containing ZFO, and the reaction was maintained at 180℃ for 12 h. After natural cooling, the products were washed and then heat-treated at 500℃ for 30 min, yielding the composite products of ZFO/NNO nanorods (abbreviated as ZFO/NNO NRs) and ZFO/NNO microcubes (abbreviated as ZFO/NNO MCs). Scheme 1 depicts the formation routes of the catalysts, providing a brief procedural overview of the synthesis of NNO NRs/MCs, ZFO nanoparticles (ZFO NPs), and NNO/ZFO heterojunctions.

2.2. Characterization of the catalysts

The morphology and microstructure of the samples were investigated using a scanning electron microscope (SEM, S4800, Hitachi Co., Japan) and a transmission electron microscope (TEM, 2100F, JEOL Co., Japan). X-ray diffraction (XRD, AXSSM-D8, Bruker, Germany) with Cu Kα radiation was used to determine the crystal structure and phase purity of the samples. X-ray photoelectron spectroscopy (XPS) was recorded using Escalab 250Xi (Thermo Scientific Instruments, USA). UV–vis absorbance spectra were recorded using a UV-2600 instrument (Shimadzu Co., Japan) with $BaSO_4$ as the reference. Electron spin resonance (ESR) signals of the radical spin were recorded using an E500 spectrometer (Bruker Co., Germany). The 5,5-dimethyl-1-pyrroline N-oxide (DMPO) was used as a spin trap to detect hydroxyl (•OH) and superoxide ($\cdot O_2^-$) radicals. The Brunauer-Emmett-Teller (BET) surface area was obtained using the nitrogen (N_2) adsorption–desorption technique at 77 K on an ASAP 2460 (Micromeritics Co., USA) instrument.

The temperature variation of different samples under simulated solar light illumination (AM 1.5 G standards, 100 mW/cm^2, 300 W Xe lamp, PLS-SXE300D, Perfectlight Technology Co., Beijing, China) was measured with a DT-1000 infrared thermometer (Shenzhen Weirdpower Technology Co., China).

The photoelectrochemical performance of catalysts was obtained using an electrochemical station (CHI660E, Chenhua Instruments, China). A three-electrode system was used, with a saturated calomel electrode and Pt serving as the reference and counter electrodes, respectively. The electrolyte used was a 0.5 M Na_2SO_4 solution. To achieve a total dispersion, 5 mg of the sample powder was added to 2 mL of ethyl alcohol and ultrasonicated for proper mixing. The resulting dispersion was then uniformly applied onto a pre-cleaned FTO glass measuring 1 cm × 1 cm. The coated glass was used as the working electrode after being dried in air at 393 K for 48 h. Electrochemical impedance spectroscopy (EIS) was conducted in the 0.1 Hz − 1 MHz range using a 5 mV AC voltage amplitude. Mott–Schottky plots (M-S plots) were recorded at a frequency of 1000 Hz. The Nernst equation was employed to convert the measured potential to that of a normal hydrogen electrode (NHE), as follows (Qian et al., 2020):

$$E_{NHE} = E_{SCE} + 0.24 \tag{2}$$

2.3. Evaluation of pyro-photodegradation activity

The photocatalytic degradation performance of the as-prepared samples (NNO NRs, ZFO/NNO NRs, and ZFO/NNO MCs) was evaluated using the degradation of organic dye RhB. To establish adsorption–desorption equilibrium between RhB and the catalysts, a 50 mL degradation solution of RhB (10 mg·L^{-1}) was poured into a quartz beaker containing 50 mg of the as-prepared photocatalyst and stirred in darkness for 1 h. The whole system was then irradiated under simulated solar light for 180 min. A 3 mL aliquot of the suspension was collected every 30 min. The extracted solution was centrifuged at 8000 rpm and analyzed for RhB concentration using a UV–vis spectrophotometer in the range of 450–650 nm. The degradation performance of the catalysts is usually expressed by the relative concentration of the dye and is calculated using the following formula:

$$X = \frac{C}{C_0} \times 100\% \tag{3}$$

Here, C_0 and C represent the RhB contents at times 0 and t, respectively. To investigate the synergistic effects of light and heat on the catalytic reactions, water was circulated around the reactor to control the solution temperature. During the catalytic degradation process, a thermocouple monitored the temperature, which was influenced by both light irradiation and circulating water. Scheme 2 illustrates the pyro-photocatalysis experimental setup, including the temperature and dT/dt profiles of the RhB solution.

2.4. Theoretical calculation

Density functional theory (DFT) calculations base on the first-principles approach were performed by CASTEP program (Cambridge Sequential Total Energy Package). A Perdew–Burke–Ernzerhof (PBE) function based on the Generalized Gradient Approximation (GGA) was used for this computational procedure. Projected augmented wave (PAW) potentials were employed to describe the ionic cores and represent valence electrons using a plane wave basis set with a kinetic energy cutoff of 520 eV (Modak et al., 2016). Partial occupancies of the Kohn-Sham orbitals were allowed with a Gaussian smearing method and a width of 0.05 eV. Electronic convergence was achieved when the energy change was less than 10^{-5} eV. Geometry optimization was considered converged when the energy change was smaller than 0.05 eV•Å^{-1}. A

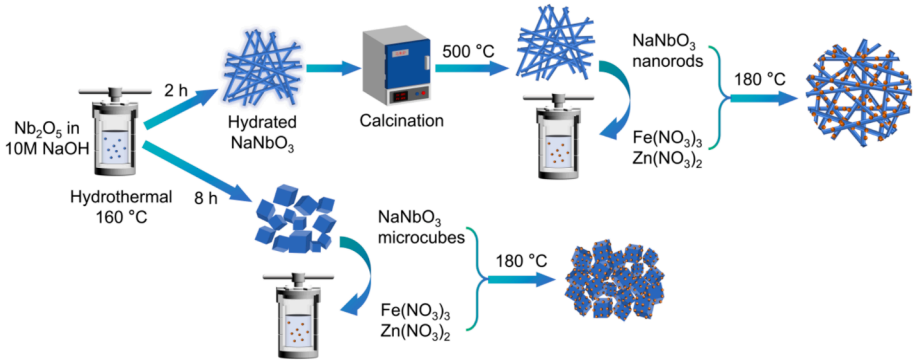

Scheme 1. A schematic illustration of the synthetic process of the ZFO/NNO composites.

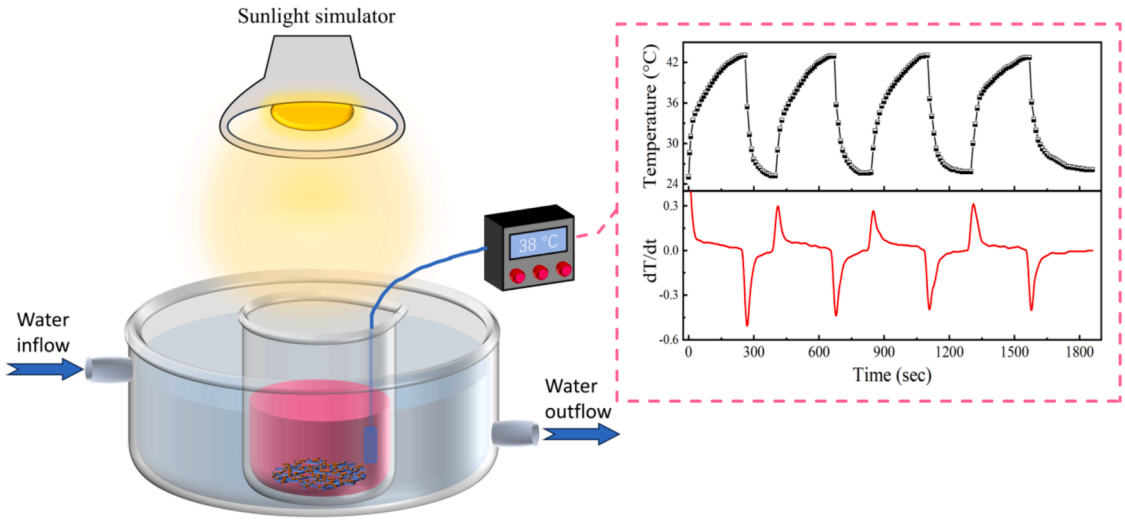

Scheme 2. The schematic diagram of pyro-photocatalysis and temperature profile of the RhB solution under simulated solar light.

vacuum spacing of 18 Å was applied in a direction perpendicular to the plane of the structure. Brillouin zone integration was performed using a 2 × 2 × 1 Monkhorst-Pack k-point mesh for the structure.

3. Results and discussion

3.1. Material characterization

Scheme 1 shows the schematic illustration of the hierarchical ZFO/NNO heterojunction synthesis process. Perovskite NNO NRs were synthesized via a two-step hydrothermal and calcination process, using Nb_2O_5 and NaOH as precursors. NNO materials with two different morphologies (nanorods and microcubes) could be obtained by adjusting the hydrothermal reaction times. After being mixed with a zinc and iron source for 2 h under magnetic stirring, both zinc and iron ions were deposited onto the surface of the NNO. Due to the good chemical stability of NNO NRs, ZFO NPs were grown in situ on them. The crystal phase and morphologies of pure NNO and ZFO, as well as ZFO/NNO composites, could be directly observed via XRD, SEM, and TEM images.

Fig. 1(a) shows the XRD patterns of the prepared samples (NNO, ZFO, ZFO/NNO NRs, and ZFO/NNO MCs). The NNO NRs diffraction pattern exhibited strong peaks at 2θ values of 22.9°, 32.6°, 46.5°, 52.6°, 58.1°, and 68.1°, which perfectly matched the reference pattern of orthorhombic NNO (JCPDS 33-1270). This result confirmed the successful synthesis of NNO using low-temperature hydrothermal followed by calcination (Yamazoe et al., 2013). The pattern of the ZFO sample (after being heat-treated at 500℃ for 30 min) showed main diffraction peaks at 2θ values of 29.9°, 35.3°, 42.8°, 53.1°, 56.6°, and 62.2°, which corresponded to cubic ZFO (JCPDS 22-1012). The corresponding crystal planes for the diffraction angles were labelled in Fig. 1(a). Both ZFO/NNO NRs and MCs exhibited XRD patterns consistent with the superposition of the two-component phases of ZFO and NNO. No diffraction peaks from impurities were observed, indicating the absence of a chemical reaction between NNO and ZFO during the solvothermal process. Furthermore, the results of the FWHM (Full Width at Half Maximum) of the primary diffraction peaks of NNO and ZFO, the grain size, and the mass percentage of the two phases in the composite were presented in Figure S1 of the Supplementary Materials.

FESEM images in Fig. 1(b) confirm the successful synthesis of bare NNO with a nanorod-like morphology and relatively smooth surface, consistent with previous literature (Zhu et al., 2006). Fig. 1(c) shows that pure ZFO products consisted of slightly aggregated nanoparticles, requiring further analysis using TEM for more accurate size determination. Fig. 1(d) and (e) show ZFO/NNO composites where ZFO NPs are well-distributed on the surface of NNO NRs and MCs, respectively. The inset of Fig. 1(e) shows that the bare NNO products have a cube-like morphology with smooth surfaces. Notably, the absence of morphological alterations in the products suggests the successful preservation of their original form despite the incorporation of ZFO. This finding further confirms the successful synthesis of ZFO/NNO composites.

The microstructure and chemical composition of the ZFO/NNO nanorod composites were analyzed by TEM. Fig. 2(a) shows abundant ZFO NPs loaded onto the surface of NNO NRs. The NNO NRs exhibited an average diameter of approximately 100 nm, as illustrated in Fig. S2 (a) of the supplementary materials. The inset reveals the ZFO NPs slightly aggregated structure with a mean size of approximately 10–20 nm (see Fig. S2 (b)). Fig. 2(b) shows the high resolution transmission electron microscopy (HRTEM) image of the ZFO/NNO NRs. Two distinct lattice fringes were observed, with lattice spacings of 0.271 nm and 0.255 nm, which can be assigned to the (141) plane of NNO and the (311) plane of ZFO, respectively. Furthermore, the high-magnification annular dark-field image and corresponding scanning The TEM-EDS images (Fig. 2(c)-(e)) demonstrated that the product is composed of the elements sodium (Na), niobium (Nb), zinc (Zn), iron (Fe), and oxygen (O). These findings collectively suggest that well-formed ZFO/NNO composites were created between ZFO NPs and NNO NRs. The mass and atomic fraction percentages of the elements were determined by means of TEM-EDS (TEM energy dispersive spectrometer). The results are presented in Figure S3 of the Supplementary Materials.

Due to the presence of surface-reactive sites, specific surface area and pore size are known to significantly influence the photocatalytic activity of materials. The variety of surface areas was determined by measuring nitrogen adsorption–desorption isotherms. As shown in Fig. 3(a), all samples exhibited type IV isotherms with H3 hysteresis loops (Xiao et al., 2015), characteristic of mesoporous materials with gas (liquid) adsorption capability. Based on the results, the ZFO/NNO NRs composite showed a higher specific surface area (S_{BET}) compared to pristine NNO MCs, ZFO/NNO NRs and ZFO/NNO MCs. This finding suggests that the composite structure consisting of nanorods and nanoparticles can provide a larger surface area, offering more active sites for the reaction resulting in a stronger photocatalytic performance at the interface (Zhao et al., 2019; Zhu et al., 2020). Fig. 3(b) shows the pore size distribution of the synthesized catalysts. NNO NRs exhibited a wide distribution, indicating the presence of irregularly stacked nanorods. The incorporation of ZFO NPs led to a narrower distribution in ZFO/NNO NRs, possibly due to partial blockage of inter-rod spaces by ZFO. The values of BET surface area and pore volume of different samples are listed in Table 1.

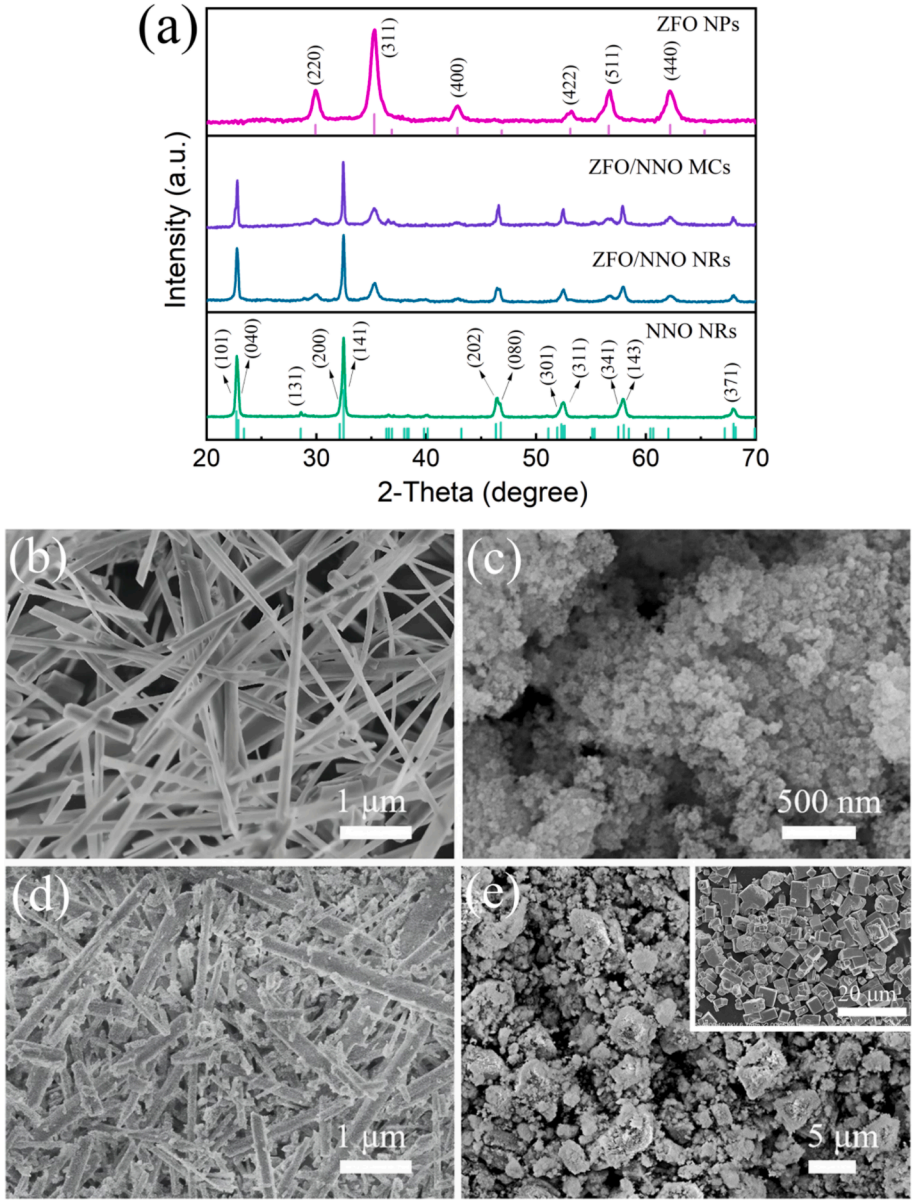

Fig. 1. XRD patterns (a) and morphologies of NNO NRs (b), ZFO NPs (c), ZFO/NNO NRs (d), and ZFO/NNO MCs (e). The inset of (e) is the morphology picture of NNO MCs.

XPS analysis was performed to determine the elemental composition and chemical state of NNO, ZFO, and ZFO/NNO NRs. The C 1s peak at 284.8 eV was used for calibration. Fig. 4(a) depicts the complete survey XPS scans of NNO, ZFO and ZFO/NNO NRs, verifying the presence of Na, Nb, Zn, Fe, and O elements. Fig. 4(b) shows high-resolution XPS spectra of Na 1s in NNO and ZFO/NNO composites. The binding energies were 1071.6 eV and 1072.1 eV for NNO and ZFO/NNO, respectively, corresponding to Na^{+}. Fig. 4(c) displays the Nb 3d XPS spectra, which exhibited a spin–orbit doublet with peaks at 206.6 eV and 209.3 eV for Nb $3d_{5/2}$ and Nb $3d_{3/2}$, respectively. These peaks confirmed the Nb^{5+} oxidation state in NNO. As shown in Fig. 4(d), the peaks observed at 1021.6 and 1044.6 eV corresponded to Zn $2p_{3/2}$ and Zn $2p_{1/2}$, respectively, indicating the existence of Zn^{2+} in $ZnFe_2O_4$. In Fig. 4(e), the XPS peaks located at 711.8 and 725.6 eV for Fe 2p were attributed to the spectra of Fe $2p_{3/2}$ and Fe $2p_{1/2}$, indicating the presence of Fe^{3+} ion. The two shake-up satellite signals located at ~ 719.7 and 733.6 eV confirm the presence of the element Fe in the synthesized materials as Fe^{3+}. Furthermore, the binding energies of Na 1 s and Nb 3d in ZFO/NNO NRs composite exhibited a mild shift towards the positive side as compared to those in pure NNO. Conversely, in the ZFO/NNO NRs composite, the peaks of Zn 2p and Fe 2p shifted to lower binding energies compared to those of the pristine ZFO. These binding energy shifts for the heterojunction components might be explained by the strong interaction between ZFO and NNO. The enhancement (upward shift) of binding energy theoretically indicated a weakened electron screening effect caused by the decreased electron concentration. Conversely, an increase in electron concentration led to a decrease (downward shift) in binding energy due to the promoted electron screening effect (Xu et al., 2021; Li et al., 2023). Consequently, in this case, it is highly conceivable that the observed upward and downward shifts of binding energy result from the increased electron concentration of ZFO and decreased electron concentration of NNO caused by the strong interaction based on the interfacial charge transfer from NNO to ZFO. In addition, high-resolution XPS O 1s spectra of the pristine NNO, ZFO and heterojunction samples were shown in Figure S4 of the Supplementary Materials.

Light absorption is crucial for semiconductor photocatalysts. Fig. 5 (a) shows the UV–Vis absorbance spectra of the prepared NNO, ZFO, and ZFO/NNO composites. The unmodified NNO exhibited a strong UV

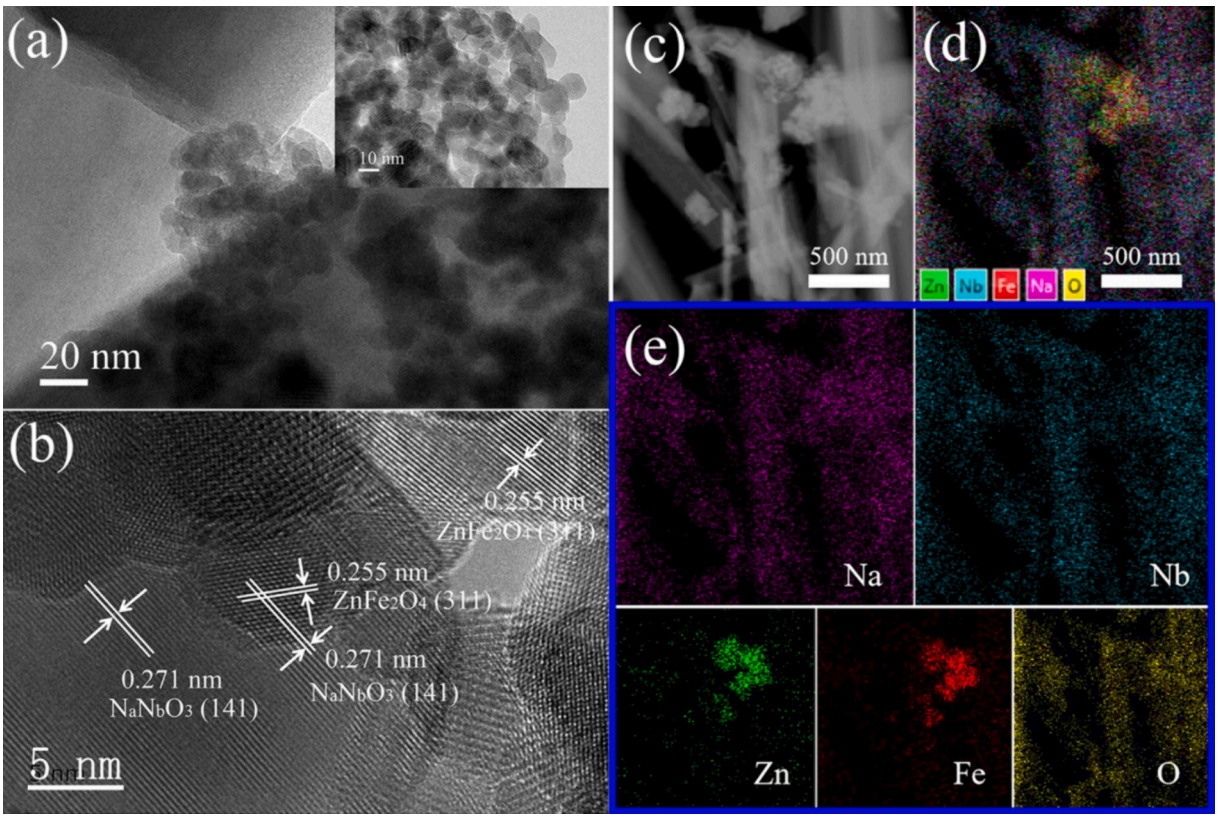

Fig. 2. TEM images of ZFO/NNO NRs (a) and ZFO NPs (inset); HRTEM (b) and scanning TEM-EDS images (c, d, e) of ZFO/NNO NRs.

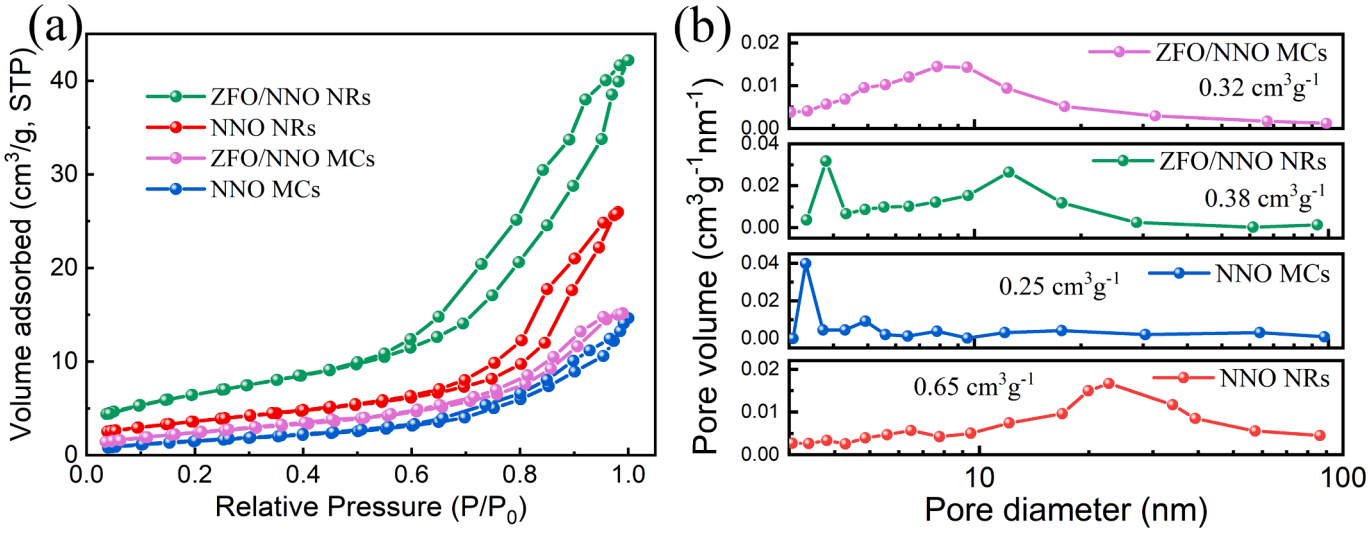

Fig. 3. N_2 adsorption–desorption isotherms (a) and pore size distribution plots (b) of the as-prepared catalysts.

Table 1
The BET surface area and pore volume of different samples.

Samples	NNO NRs	NNO MCs	ZFO/NNO NRs	ZFO/NNO MCs
S_{BET} (m^2/g)	12.3	4.6	24.9	5.4
Pore volume (cm^3/g)	0.65	0.25	0.38	0.32

absorption edge at around 375 nm, as shown in its UV–Vis absorbance spectrum. Pure ZFO NPs exhibited broad light absorption from UV to visible light (below 650 nm), potentially beneficial for a wider range of light-activated reactions. In the case of ZFO/NNO composites, the UV–Vis absorbance spectra showed a combined absorption feature of ZFO and NNO. Additionally, ZFO/NNO NRs showed a stronger absorption compared to the ZFO/NNO MCs composite. This could be attributed to the agglomerated ZFO NPs covering the surface of NNO MCs, which reduced scattering of visible light, leading to a decrease in the absorption intensity of the composites (Zhao et al., 2019). The results of UV–Vis DRS indicated that the heterojunction broadened the photo-

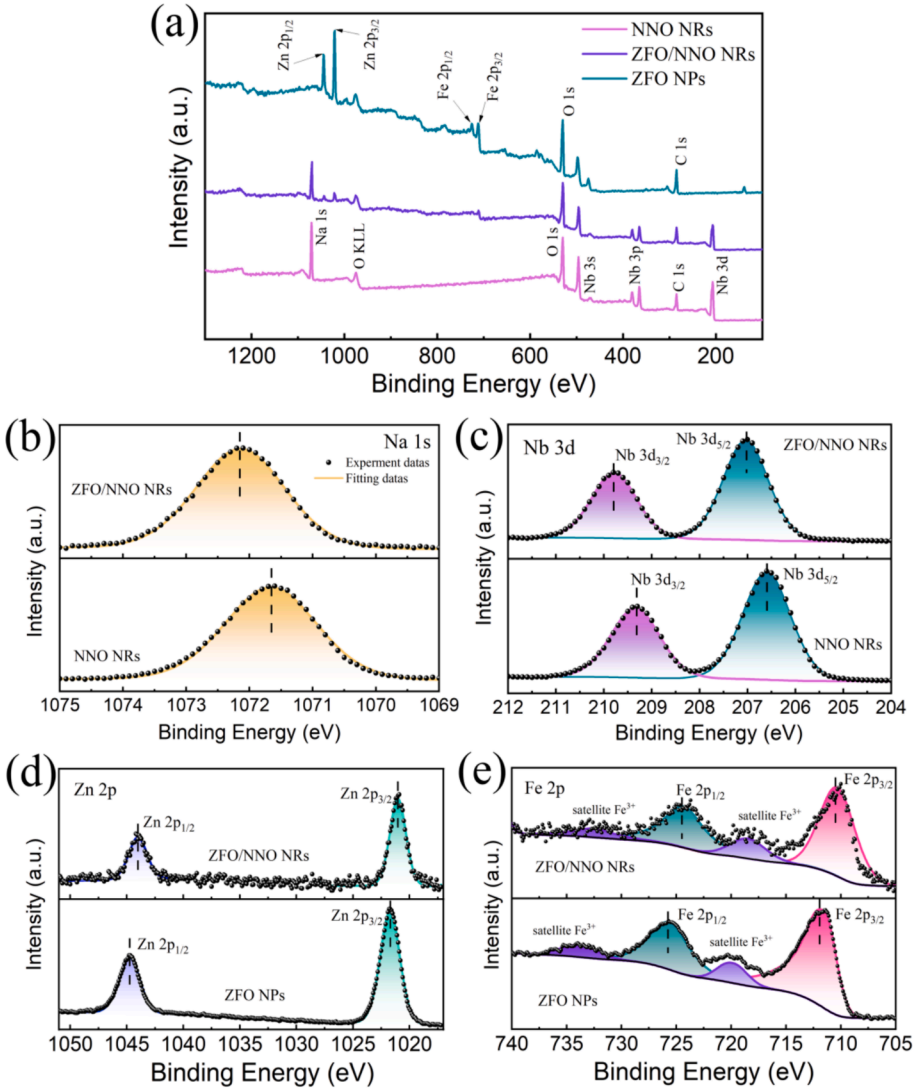

Fig. 4. XPS fully scanned spectra (a) and high-resolution XPS spectra of Na 1s (b), Nb 3d (c), Zn 2p (d). and Fe 2p (e) in NNO, ZFO and ZFO/NNO NRs.

absorption range and improved the limited light absorption ability of NNO, which is highly advantageous in the activation of more charge carriers.

Furthermore, the optical band gap of the samples could be estimated from plots of $(\alpha h\nu)^{1/2}$ vs. photon energy ($h\nu$)(Fig. 5(b)) based on the Kubelka-Munk method and Tauc's equation as follows (Khan et al., 2020):

$$(\alpha h\nu)^{\frac{1}{n}} = A(h\nu - E_g) \tag{4}$$

Here, A, α, h, ν, and E_g represent the absorption constant, absorption coefficient, Planck constant, photon frequency, and bandgap energy, respectively. For both NNO and ZFO, the value of n is 2, which is characteristic of an indirect bandgap semiconductor (Fuentes-Pérez et al., 2021; Hasan and Azhdar, 2023; Zhang et al., 2022). Therefore, the band gaps (E_g) of NNO and ZFO were 3.33 and 1.85 eV, respectively. This conclusion aligns with the incident photon energy corresponding to the absorption edge observed in the optical absorption spectra (Fig. 5 (a)) of the samples. Furthermore, the Tauc plots of ZFO/NNO NRs and ZFO/NNR MCs were generated and presented in the Supplementary Materials (see Figure S5).

Building on its light absorption properties, ZFO is a typical photothermal agent that absorbs light energy and converts it into heat energy (Yang et al., 2021). The temperature changes of the samples' surfaces were recorded with an infrared thermometer to quantify the photothermal effect, as shown in Fig. 5(c). The surface temperature of pristine NNO NRs steadily increased from the ambient temperature of 24°C to reach ~ 40 °C within 20 min under simulated solar light irradiation. In contrast, ZFO/NNO NRs composite exhibited a rapid temperature rise within 200 s, followed by a gradual increase to a maximum temperature exceeding 55 °C within 20 min. These results demonstrate that the addition of ZFO could enhance both visible light absorption and thermal conversion (Li et al., 2023).

3.2. *Pyro-photocatalytic degradation performance*

To examine the critical role of the photocatalyst, a control experiment was conducted. As shown in Fig. 6(a), negligible degradation of the RhB solution occurred under simultaneous light irradiation and temperature fluctuations in the absence of catalysts. It is well-known that RhB dye is highly stable, and the pyrolysis of organic molecules typically occurs at elevated temperatures (200–700 °C) (Inyang and Dickenson, 2015). Moreover, no decomposition of the RhB solution was observed, even with the NNO or ZFO/NNO pyrocatalysts under dark conditions. This is attributed to the limited intrinsic excitation in semiconductors, resulting in insufficient excitons to generate active free radicals (Luo et al., 2022). Then, the photo-pyrocatalytic performance of the ZFO/NNO heterojunctions under light irradiation and temperature

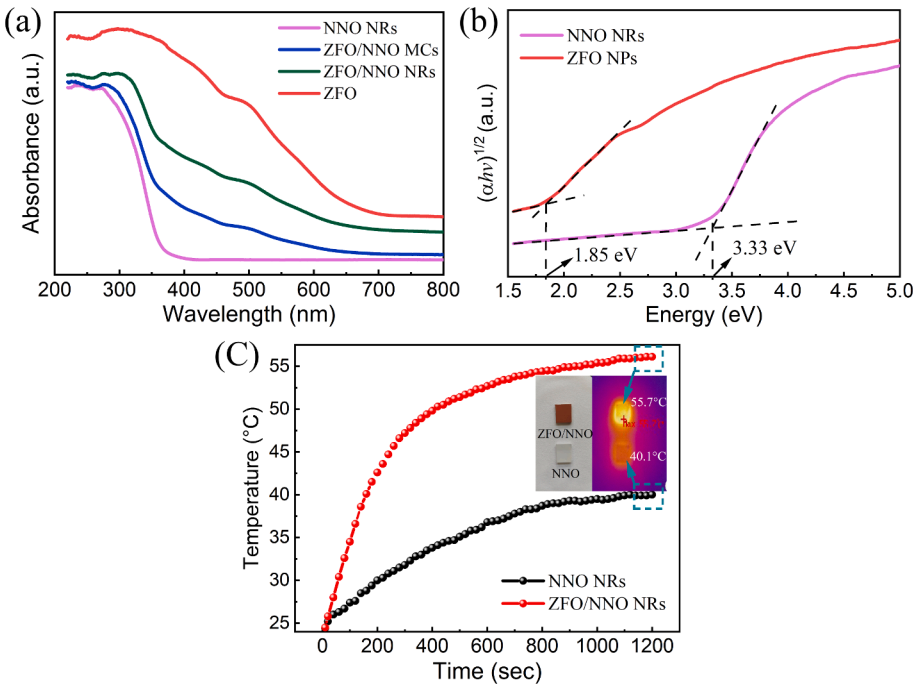

Fig. 5. (a) UV–vis absorbance spectra, (b) plots of $(\alpha hv)^{1/2}$ vs. hv of the prepared NNO, ZFO, and ZFO/NNO composites, and (c) temperature–time profile of the surface of the sample under simulated solar light irradiation. The inset shows thermal imaging photos corresponding to the hottest temperatures.

fluctuations was investigated for their combined effects on RhB degradation. The experimental conditions consisted of simultaneous light irradiation and temperature fluctuations, as well as light irradiation alone. Fig. 6(b) demonstrated the degradation performance of RhB using NNO, ZFO, and ZFO/NNO heterojunctions as photo-pyrocatalysts, respectively. Evidently, the RhB exhibited some degradation under light conditions regardless of the catalyst sample used. In particular, the degradation of RhB was notably improved under conditions of temperature fluctuation, which implied that utilizing temperature fluctuations to promote the degradation of dyes for the pyroelectric catalysts is an effective approach. Fig. 6(c) and (d) display the kinetic plots of the degradation reactions corresponding to Fig. 6(a) and (d), respectively. These reactions were simulated using the Langmuir-Hinshelwood kinetic method. The equation for the Langmuir-Hinshelwood model is as follows (Goutham et al., 2022):

$$-\ln(C/C_0) = kt \tag{5}$$

The natural logarithm of the concentration ratio ($-\ln(C/C_0)$) exhibits a linear relationship with time t, where k represents the reaction's kinetic constant. As shown in Fig. 6(d), the ZFO/NNO NRs composite exhibited superior photocatalytic activity under light irradiation with constant temperature, compared to single ZFO and NNO catalysts. This could be attributed to the broad absorption of the solar spectrum by ZFO and the formation of a heterojunction between ZFO and NNO. When temperature fluctuated, the equilibrium between the polarization charges and the compensation charges bound on the pyroelectric material surface was disrupted, leading to the excess compensation charges during heating and the migration of charges in solution towards the catalyst surface during cooling, both of which can participate in the catalytic reaction (Qiao et al., 2021). Fig. 6(b) and (d) show that ZFO/NNO NRs heterojunction demonstrated the highest catalytic performance (the highest percentage degradation and the fastest rate constant) under the combined effects of light irradiation and temperature variations. Accordingly, the presence of pyroelectric NNO and temperature variation are indispensable for the photo-pyrocatalytic decomposition of dye solution.

The reusability of photocatalysts is essential for practical applications, especially considering their separation and stability. To assess the reusability of ZFO/NNO NRs composite for practical applications, their photocatalytic stability under cyclic degradation with light irradiation and temperature variation was investigated. The ZFO/NNO NRs heterojunction exhibited good stability, as shown by the slight (only 6 %) decrease in degradation efficiency observed after five consecutive cycles (Fig. 7(a)). XRD patterns of the samples before and after the reaction cycle (Fig. 7(b)) showed almost identical peaks, indicating that the crystal structure remained largely unchanged. In summary, these results suggest that ZFO/NNO heterojunctions exhibit stability in the photocatalytic degradation of RhB dye. Additionally, the magnetic properties of the ZFO/NNO catalyst were evaluated. When a magnet was placed near the bottle containing the catalyst dispersion for one hour, the ZFO/NNO catalyst responded to the magnet by moving towards the inner wall of the bottle (Fig. 7(c)), suggesting that the introduction of ZFO made the catalyst magnetic. The complexation of catalysts with magnetic particles offers a solution to the challenge of separating photocatalysts from degradation solutions.

3.3. Radical and hole-trapping experiments

Identifying the primary active species generated by photocatalysts is crucial for understanding the degradation mechanism. To identify the primary reactive species involved, different radical scavengers were added to the RhB solution: *tert*-butanol (TBA) for hydroxyl radicals (•OH), p-benzoquinone (BQ) for superoxide radicals ($\cdot O_2^-$), and ethylenediaminetetraacetate (EDTA) for holes (h^+) (Yang et al., 2021; Zhang et al., 2023; Sun et al., 2021; Xiao et al., 2015). As shown in Fig. 8(a), the percentage degradation of RhB after 3 h of photocatalysis varied in their suppressive effect, implying that the active species include hydroxyl radicals, superoxide radicals, and holes. With the addition of BQ, the degradation ratio was only 23 %, indicating that the superoxide radical was the primary reactive species during the degradation process. We found that 27 % of RhB was degraded after adding EDTA to capture h^+, suggesting that h^+ also played an important role in the degradation of RhB. The degradation ratio of RhB showed slight suppression after the addition of TBA, implying that the influence of hydroxyl radicals was

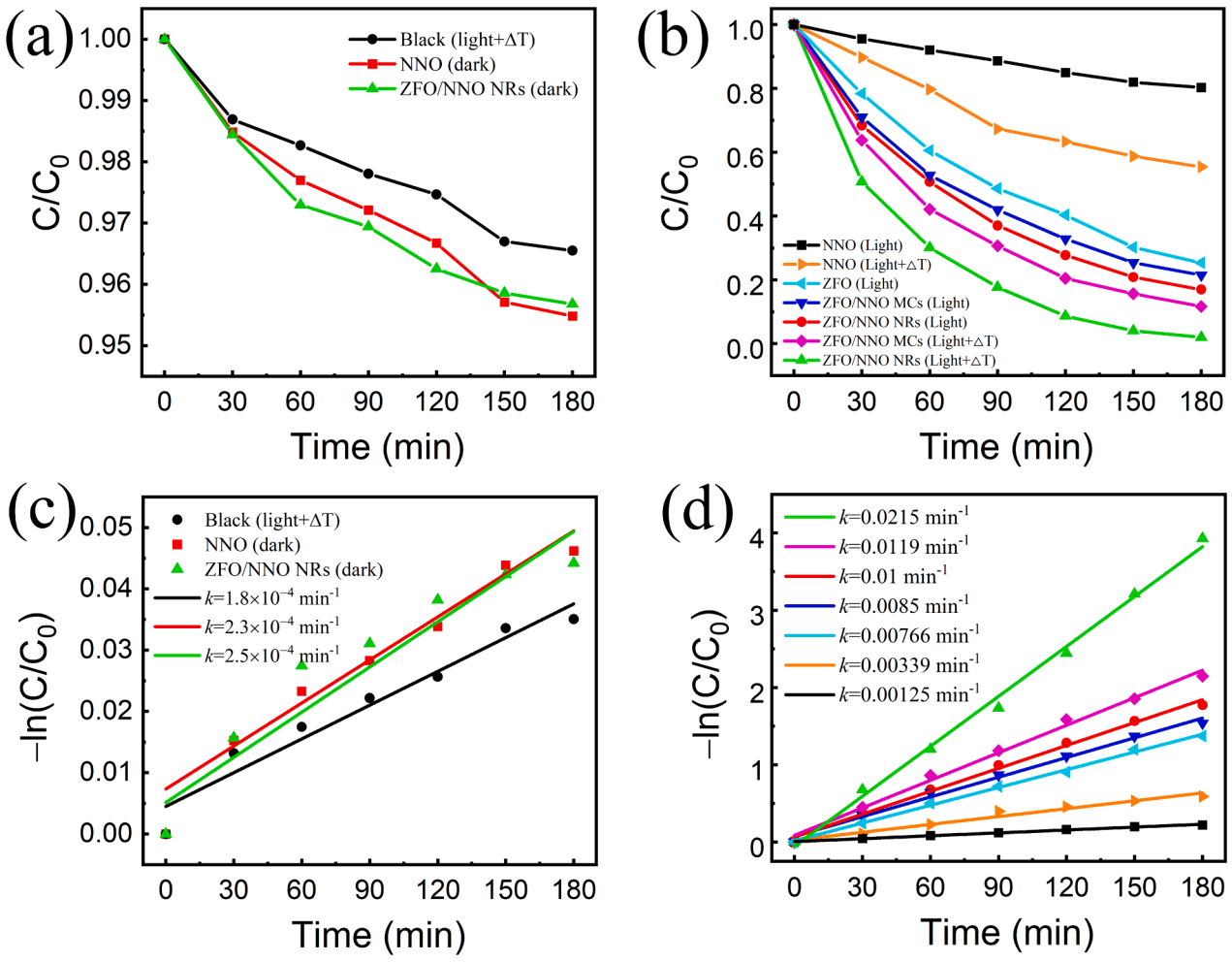

Fig. 6. Photocatalytic performance: the concentration–time plots of RhB solution under dark (a) and light irradiation and temperature variation together (b), the linear fitting curves of kinetic rate constants (c) and (d) calculated from (a) and (b), respectively.

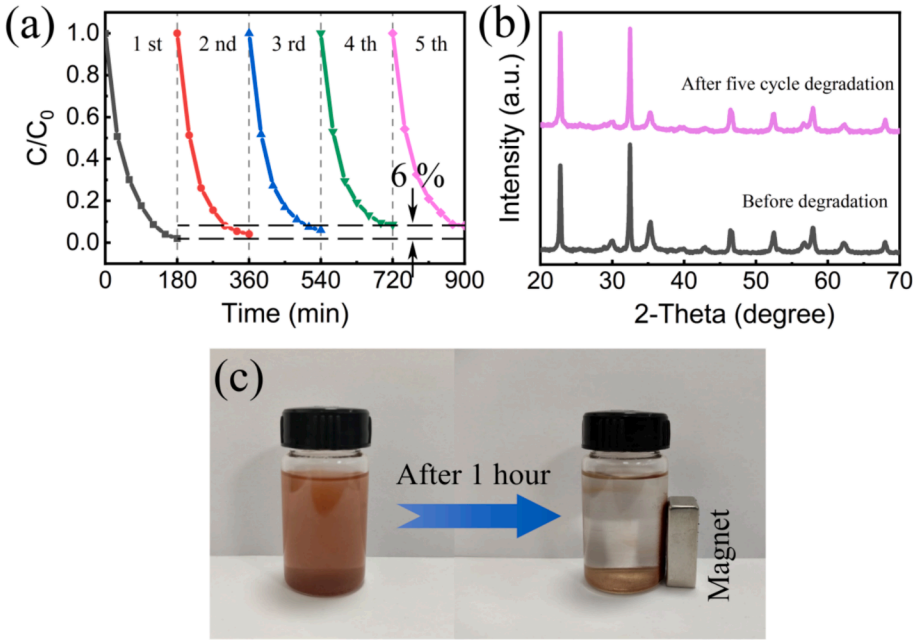

Fig. 7. (a) The degradation cyclic performance; (b) the XRD patterns of the ZFO/NNO catalyst before and after the degradation reaction; (c) a photograph of the catalyst held by a magnet.

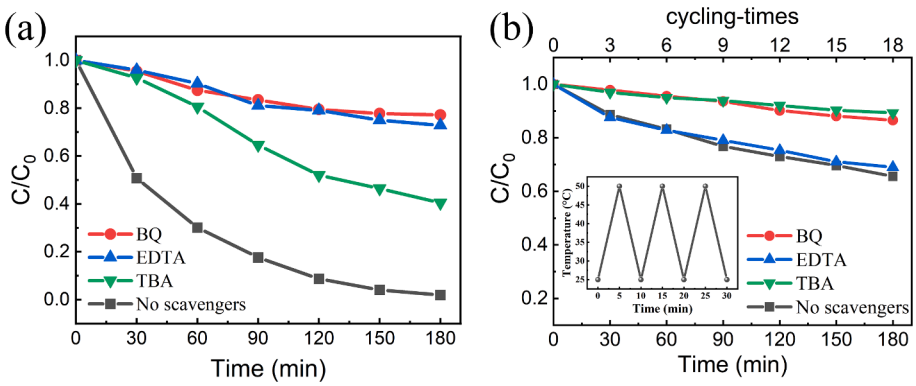

Fig. 8. Radicals-trapping experiments of (a) ZFO/NNO NRs under light irradiation and (b) NNO NRs under temperature cycling with and without radical scavengers. The inset of (b) is the setup temperature variation for cold-hot cycles.

moderate for photo-pyro-catalytic degradation.

To understand the role of temperature fluctuations, an RhB degradation experiment with NNO NRs and radical scavengers was conducted in the dark to avoid the production of photogenerated carriers. The temperature cycling was achieved with a temperature-controllable water bath device (HH-S1A, Guangzhou Instrument Manufacturing Co., LTD, China), set in the temperature variation range of 25–50°C at 5 °C/min. Fig. 8(b) shows the influence of different scavengers on the degradation rate of RhB in the NNO pyro-catalytic degradation process. After the addition of these scavengers, the degradation efficiency was inhibited to some extent. Among them, the degradation efficiency decreased significantly after adding BQ and TBA, indicating that $\cdot O_2^-$ and •OH were responsible for the main degradation reaction. The reaction process can be inferred as follows.

$$NaNbO_3 \xrightarrow{\Delta T} NaNbO_3(q^+ + q^-)$$

$$O_2 + q^- \rightarrow \cdot O_2^-$$

$$OH^- + q^+ \rightarrow \cdot OH$$

$$\cdot O_2^- and \cdot OH + Dye \rightarrow Decomposition production$$

3.4. Pyro-Photocatalytic mechanism

To understand the impact of the heterojunction on charge separation, photoelectrochemical measurements were performed to analyze the charge transfer mechanism of the samples. Fig. 9(a) displays the Nyquist plots of electrochemical impedance spectroscopy (EIS) for NNO and ZFO/NNO NRs, measured using an electrochemical workstation. The arc radius of the analyzed Nyquist curve is generally considered proportional to the charge transfer impedance at the interface (Zhang et al., 2022; Xu et al., 2021). As shown in Fig. 9(a), the arc radius of ZFO/NNO NRs was smaller than that of NNO, with the smallest radius observed under light irradiation and temperature fluctuations. This indicated the lowest charge transfer resistance, which translated to the highest separation and transfer efficiency of charge carriers at this time.

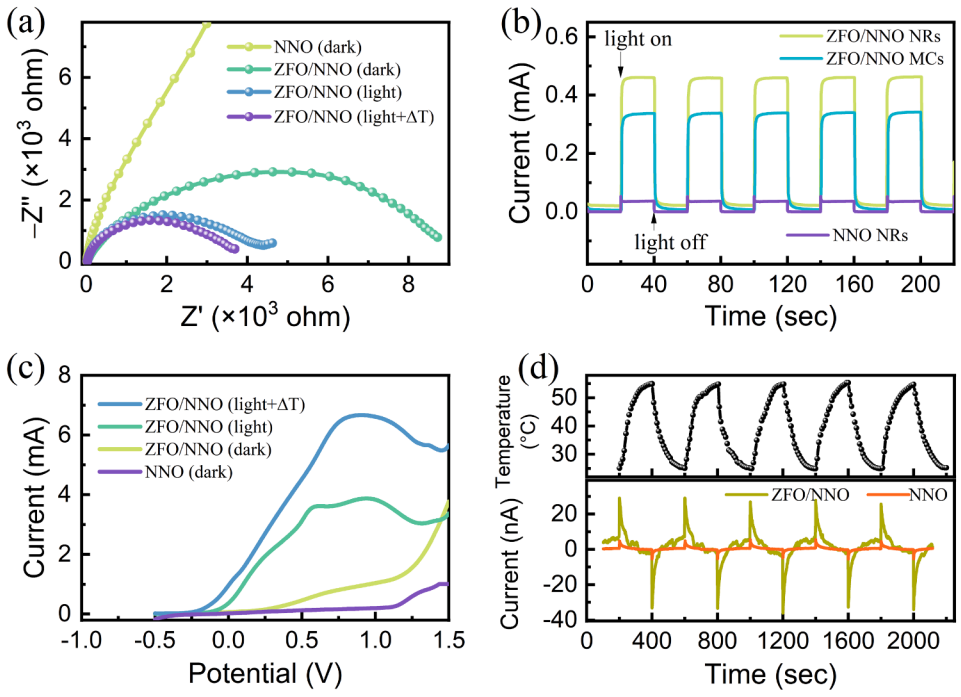

Fig. 9. (a) Nyquist plots of EIS, (b) transient photocurrent response curves, (c) LSV curves, and (d) pyroelectric current–time curves of NNO and ZFO/NNO NRs composite.

Therefore, the combination of ZFO with NNO and the pyroelectric effect stimulated by photothermal excitation reduced the interfacial charge transfer resistance and enhanced the separation and utilization efficiency of the charge carriers, ultimately improving photocatalytic performance.

To further investigate the reproducibility and stability of photocatalysts in response to light, a transient photocurrent response experiment was conducted under chopped-light irradiation (light switched on and off every 20 s). Fig. 9(b) shows the current–time (*I-t*) responses of the photoelectrodes under chopped-light irradiation. The responses

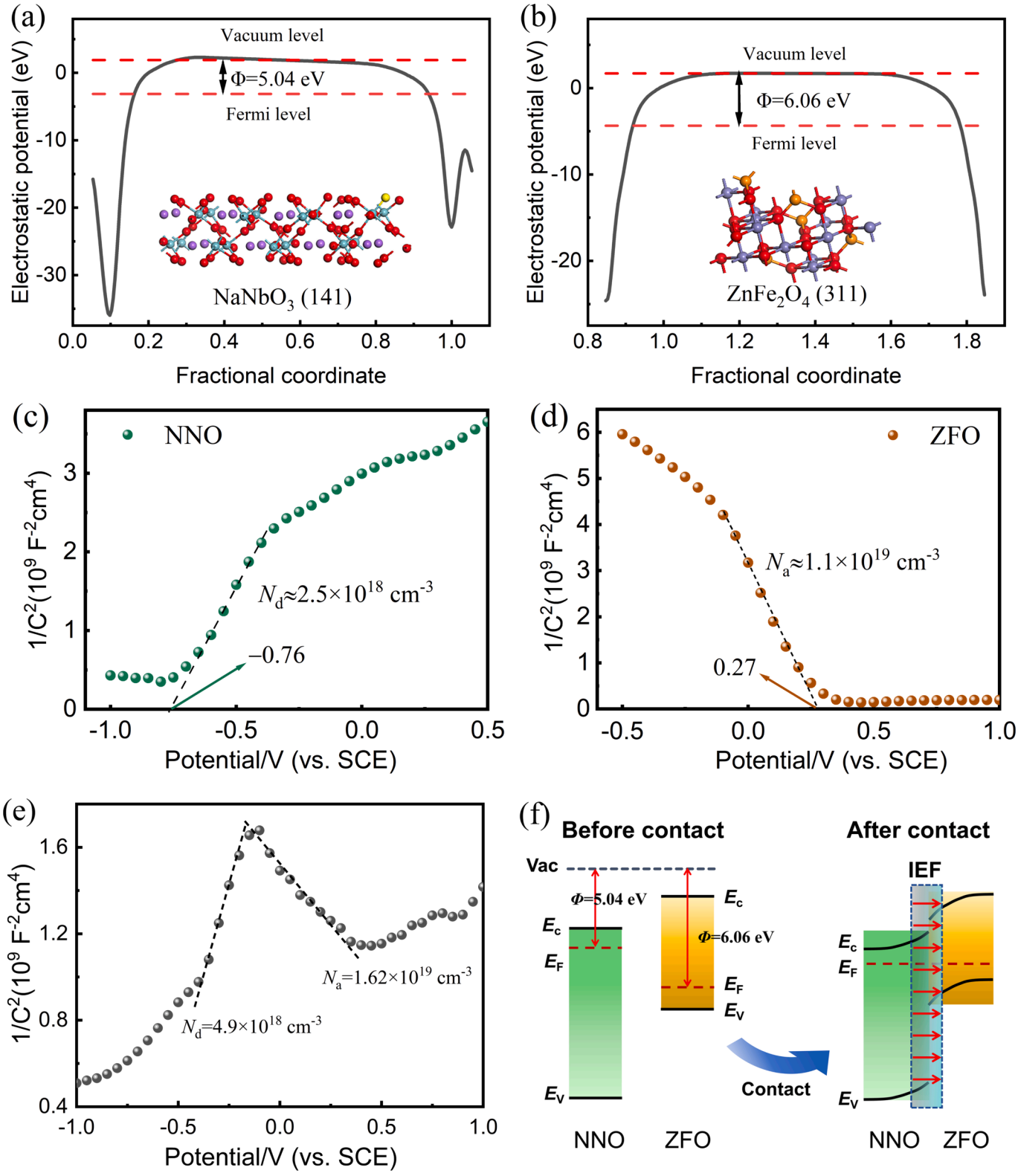

Fig. 10. Electrostatic potentials of (a) NNO and (b) ZFO determined by DFT; Mott-Schottky plots of (c) NNO NRs, (d) ZFO and (e) ZFO/NNO NRs composite collected under light irradiation; (f) the energy level arrangement of NNO and ZFO before and after contact.

were stable, reproducible, and showed a clear response to the light on–off cycles. Compared to the other samples, the ZFO/NNO NRs heterostructure showed the highest photocurrent intensity. The photocurrent response curve of the ZFO NPs electrode was presented in the Supplementary Materials, see Figure S6. Fig. 9(c) displays the linear sweep voltammetry (LSV) curves of NNO and ZFO/NNO NRs. The ZFO/NNO electrode exhibited a higher current response under light irradiation compared to darkness. Additionally, an increase in temperature during the process resulted in the maximum photocurrent being achieved at the same bias voltage. The experimental results of the photocurrent response discussed above suggest that the ZFO/NNO catalyst generated a significant number of electrons and holes, as well as compensating charge on the catalyst surface that could be excited and transferred, under the combined effect of light and temperature change (Goutham et al., 2022). This allowed for greater participation of charge carriers generated by photoexcitation and the pyroelectric effect in the photocatalytic reaction.

The photocatalytic performance observed in Fig. 6 was consistent with these findings. This could be attributed to the binary heterostructure and dimensional structure of ZFO/NNO NRs. The heterostructure promoted photogenerated electron-hole separation and charge transfer, leading to a higher number of charge carriers participating in the photocatalytic reaction. Additionally, the presence of NNO in the heterojunction played a crucial role due to its pyroelectric effect. Fig. 9(d) illustrates the temperature and pyroelectric current–time curves of NNO and ZFO/NNO catalysts under cold-hot cycle excitations. Temperature cycling between 25–55 °C in the dark environment was achieved using the laboratory's own hot/cold cycling apparatus, which avoids the production of photogenerated carriers. Compared to photocurrents, the pyroelectric currents of both NNO and ZFO/NNO catalysts were much less intense. They were rapidly excited when the catalyst temperature increased or decreased but quickly diminished when the temperature stabilized. The current is generated by the compensation charges in the solution, which migrates between the two poles driven by the pyroelectric field. The current intensity, according to equation (1) is directly proportional to the rate of temperature change (Yang et al., 2012; Yang et al., 2012). This pyroelectric field likely promotes the separation of charge carriers within the semiconductor photocatalyst and accelerates their migration toward the surface. This, in turn, leads to the generation of reactive radicals that participate in redox reactions with dye molecules. Furthermore, the PL spectra of the pristine NNO, ZFO and heterojunction samples were recorded using an Edinburgh FS5 fluorescence spectrophotometer, the results of which were presented in Figure S7 of the Supplementary Materials.

Density functional theory was further investigated to understand the interface charge transfer between $NaNbO_3$ and ZFO. Fig. 10(a) and (b) show the calculated theoretical work functions of NNO (5.04 eV) and ZFO (6.06 eV). Since the Fermi level of NNO was higher than that of ZFO, electrons transferred from NNO to ZFO upon contact until their Fermi levels reached equilibrium. Subsequently, ZFO and NNO were negatively and positively charged respectively, forming an internal electric field (IEF) from NNO to ZFO. The charge transfer process derived from these findings aligned with the XPS characterization results. With the existence of IEF, the electron-hole pairs on NNO and ZFO were separated from each other, and it also caused band bending at the interface of ZFO and NNO (Tian et al., 2023).

Mott-Schottky (M−S) measurements were conducted to identify semiconductor types and band structures. As shown in Fig. 10(c), the positive slope of the Mott-Schottky plot for the NNO NRs electrode indicated its n-type character. Extrapolating the linear region to the x-axis where $C^{-2} = 0$ yielded an E_{fb} of approximately − 0.76 V (vs. SCE). Similarly, the negative slope of the curve for the ZFO NPs electrode indicated a p-type characteristic, with an E_{fb} of around 0.27 V (vs. SCE) (see Fig. 10(d)) (Li et al., 2023). The ZFO/NNO composite exhibited an inverted V-shaped curve in Fig. 10(e), signifying the formation of a p–n heterojunction. In general, there is a 0.24 V difference between the SCE and the normal hydrogen electrode (NHE) (Qi et al., 2020). Moreover, the flat band potential was 0.1 ~ 0.2 eV higher than its conduction band potential (E_{CB}) for n-type semiconductors and lower than its valence band potential (E_{VB}) for p-type semiconductors. Therefore, the E_{VB} of ZFO was approximately 0.61 V (vs. NHE), and the E_{CB} of NNO was approximately −0.62 V (vs. NHE). Furthermore, the E_{VB} of NNO and the E_{CB} of ZFO were 2.71 V and −1.24 V (vs. NHE), respectively, using the following equation (Wu et al., 2019):

$$E_g = E_{VB} - E_{CB} \tag{6}$$

Based on Fig. 5(b), the bandgaps (E_g) of pure NNO and ZFO were approximately 3.33 eV and 1.85 eV, respectively.

As previously mentioned, Fig. 10(f) illustrates the energy level arrangement of NNO and ZFO before contact and the formation of an internal electric field after contact. After contacting, the energy levels of NNO and ZFO formed a type-II heterojunction structure, favorable for charge transfer and separation. The formation of the ZFO/NNO p-n heterojunction caused the Fermi levels of ZFO and NNO to align. Subsequently, an internal electric field was generated at the interface (Zhao et al., 2022). As a result, the band edge of NNO was bent upward due to electron loss, while that of ZFO was bent downward due to electron enrichment (Sudhir Ekande and Kumar, 2023). When exposed to simulated sunlight, electrons in both ZFO and NNO's valence band (VB) were excited to their empty conduction band (CB), leaving holes in the VB. ZFO/NNO exhibited a traditional type-II scheme, therefore electrons in ZFO's CB were further transferred to NNO's CB, through the p-n junction, whereas the holes in NNO's VB were transferred to ZFO's VB. Since the NNO's conduction band minimum (E_{CB}) levels (−0.62 V) were more negative than the $\cdot O_2^-/O_2$ redox potential (−0.33 eV vs. NHE), the generation of superoxide radicals was thermodynamically favorable. However, according to the theory, the valence band maximum (E_{VB}) value of ZFO (0.61 V) was lower than the $\cdot OH/OH^-$ redox potential (1.99 eV vs. NHE), making the formation of hydroxyl radicals unfavorable. This contradicted the experimental results of free radical trapping, suggesting further investigation is needed to understand the pathway of hydroxyl radical production.

The carrier concentration, which signifies the density of electron donors (N_d) in n-type semiconductors and electron acceptors (N_a) in p-type semiconductors, can be determined from the slopes of the quasi-linear regions near the E_{fb} in the Mott–Schottky plots using the following equation (Sudhir Ekande and Kumar, 2023; Soltani et al., 2020):

$$\frac{1}{C^2} = \frac{2}{e\varepsilon\varepsilon_0 N_d}\left[(V - V_{fb}) - \frac{kT}{e}\right] \tag{7}$$

Here, C represents the interface capacitance with the electrolyte, e indicates the electronic charge, ε_0 denotes the vacuum permittivity (8.85×10^{-14} F·cm^{-1}), ε represents the sample dielectric constant (i.e., 105 for NNO and 423 for ZFO) (Yu et al., 2021; Naseer et al., 2022); N_d refers to the charge-carrier concentration, V and V_{fb} are the applied and flat-band potentials respectively, k indicates the Boltzmann's constant, and T denotes the temperature. The calculated donor (N_d) concentration for the NNO NRs and acceptor (Na) concentration for the ZFO NPs were approximately 2.5×10^{18} cm^{-3} and 1.1×10^{19} cm^{-3}, respectively. The ZFO/NNO NRs composite exhibited similar trends, with N_d and N_a concentrations of around 4.9×10^{18} cm^{-3} and 1.62×10^{19} cm^{-3}, respectively. These results confirmed that the internal electric field could accelerate the separation of photogenerated electron-hole pairs toward the surface, leading to a significant increase in carrier density, resulting in more charge carriers transported to the catalyst surface to participate in redox reactions (Li et al., 2022; Sudhir Ekande and Kumar, 2023).

Based on the experimental results and energy band theory, a mechanism for the pyro-photocatalytic degradation of RhB by ZFO/NNO was proposed. The pyroelectric effect of NNO plays a crucial role due to its introduction. Fig. 11(a) illustrates the pyroelectrocatalytic process for

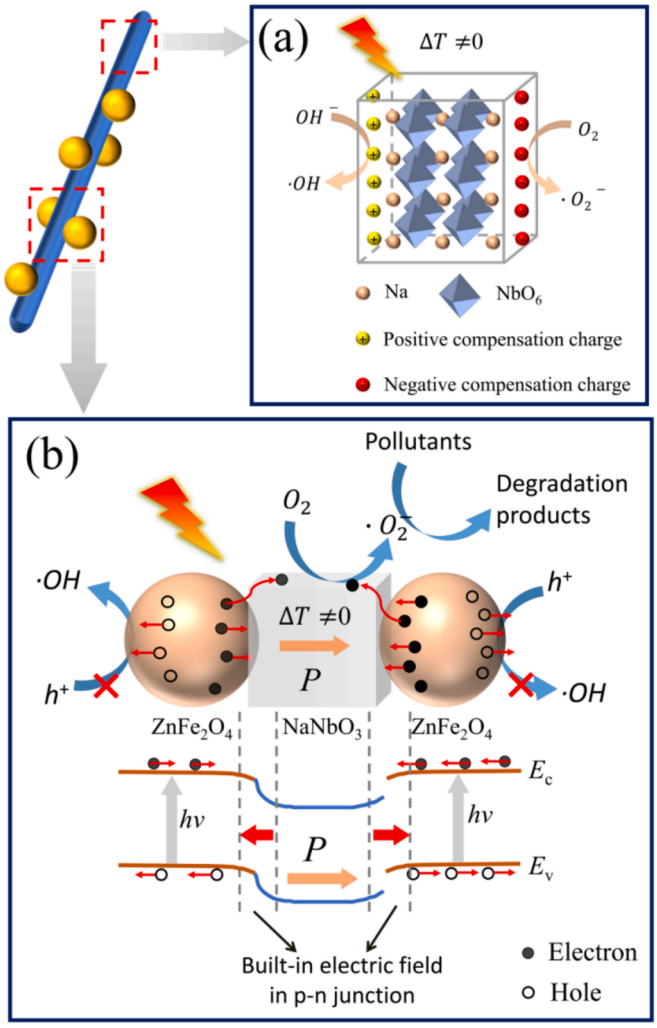

Fig. 11. The schematic diagram for the pyro-/photocatalytic mechanism of (a) NNO and (b) ZFO/NNO composites.

dye degradation. In the equilibrium state with constant temperature, surface-bound charges on the NNO surface were shielded by the shielding charges. When the temperature changed ($\Delta T \neq 0$), the pyroelectric effect altered the orientation of the electric dipoles and the spontaneous polarization intensity of NNO. This disrupted the balance between the polarization charges and the shielding charges, leading to uncompensated surface charges. Among these charges, negative charges (q^-) could rapidly combine with oxygen molecules adsorbed on the NNO surface to form superoxide radicals. Positive charges (q^+) facilitated the generation of hydroxyl radicals in the dye solution (Benke et al., 2015; Zhao et al., 2022). These strong oxidizing $\cdot O_2^-$ and •OH could further react with the dye molecules, leading to the decomposition of RhB dye in solution. Additionally, the imbalance of surface charge could desorb the decomposition products adsorbed on the catalyst surface (Liu et al., 2024).

When the ZFO/NNO composite was co-stimulated by light and heat, the synergy of the pyroelectric and the photoelectronic effects promoted the separation and transport of photogenerated carriers, and also generated the hydroxyl radicals (Wu et al., 2019; Naseer et al., 2022). As shown in Fig. 11(b), during temperature changes, NNO NRs generated a built-in electric field due to the pyroelectric effect. Under the influence of this pyroelectric potential, a positive polarization charge attracted electrons in its vicinity, resulting in the downward bending of the energy band edges. Conversely, a negative polarization charge repelled electrons in its vicinity, leading to an upward bending of the energy bands. In comparison to the equilibrium state with a constant temperature, this alteration in the degree of energy band bending disrupted the charge shielding effect and concurrently facilitated the separation and directional migration of the photogenerated electron-hole pairs. This ultimately led to the enhancement of the photocatalytic performance of ZFO/NNO composites. Additionally, the periodic pyroelectric field generated by the alternating hot and cold temperatures could change the polarization potential, preventing the saturation of the static built-in electric field (Wang et al., 2020). This ever-changing internal polarization electric field drove the carriers to move in opposite directions, suppressing the photogenerated electron-hole recombination and thus enhancing the photocatalytic performance.

4. Conclusions

In summary, a novel ZFO/NNO p-n junction photocatalyst with pyroelectric properties was successfully synthesized using a hydrothermal method. This work investigated a promising approach for dye decomposition that leverages the synergy of pyroelectric catalysis and photocatalysis in ZFO/NNO heterostructures. The incorporation of ZFO not only extended the photocatalyst's absorption spectrum into the visible light region, but its inherent photothermal effect also provided a heat source, contributing to the temperature fluctuations experienced by NNO. Photoelectrochemical measurements and PL spectra demonstrated a significant enhancement in the separation and migration efficiency of photogenerated charge carriers due to the combined effects of the built-in potential from the ZFO/NNO heterojunction and the spontaneous polarization potential of NNO. The N_2 adsorption–desorption isotherms demonstrated that the ZFO/NNO NRs exhibited a markedly larger specific surface area (24.9 m^2/g) than the ZFO/NNO MCs (5.4 m^2/g). The light absorption curves demonstrated that the ZFO/NNO NRs exhibited a narrower band gap (2.37 eV of Eg) with a more extensive visible light absorption range than the ZFO/NNO MCs (2.8 eV of Eg). Under combined light irradiation and light-induced thermal cycling, the photocatalytic rate of ZFO/NNO NRs for RhB degradation (2.15×10^{-2} min^{-1}) was more than twice its photocatalytic rate under light irradiation alone (1.0×10^{-2} min^{-1}). Additionally, it was 2.8 and 17 times higher than the rate of ZFO (7.66×10^{-3} min^{-1}) and NNO NRs (1.25×10^{-3} min^{-1}) alone, respectively. While the photocatalytic rate of RhB degradation by ZFO/NNO MCs was 1.19×10^{-2} min^{-1}. The degradation mechanism investigation suggested that the process was mainly driven by superoxide radicals and holes generated from photoexcited electrons. Radicals generated from pyroelectrically-induced charge also contributed to the degradation of dyes. The enhanced performance of ZFO/NNO under combined light and temperature changes could be attributed to several synergistic factors, including enhanced light absorption by ZFO, the establishment of the built-in electric field of the p-n junction between ZFO and NNO, and the NNO pyroelectric effect that further improved charge transfer efficiency. This "one arrow three birds" approach provided a method for rationally designing high-efficiency pyroelectric/photothermal nanostructures for photocatalysis applications, with promise for environmental remediation.

Author agreement

All authors have seen and approved the final version of the manuscript being submitted. They warrant that the article is the authors' original work, hasn't received prior publication and isn't under consideration for publication elsewhere.

CRediT authorship contribution statement

Di Zhou: Writing – original draft, Investigation, Funding acquisition, Data curation. **Xiaoju Zhou:** Writing – original draft, Methodology, Data curation. **Zhenglong Hu:** Writing – review & editing, Project administration, Funding acquisition, Conceptualization. **Lili Zheng:** Resources, Investigation, Data curation. **Yu Tian:** Methodology, Investigation, Data curation. **Yafang Tu:** Resources, Methodology,

Investigation. **Chunbo Hua:** Resources, Funding acquisition, Data curation. **Li Xue:** Validation, Methodology, Investigation. **Juan Xiong:** Writing – review & editing, Project administration, Funding acquisition, Conceptualization.

Declaration of competing interest

The authors declare that they have no known competing financial interests or personal relationships that could have appeared to influence the work reported in this paper.

Acknowledgements

This work was financially supported by the projects of National Natural Science Foundation of China (Grant No. 12304539), Natural - Science Foundation of Hubei Province (Grant No. 2022CFB518), Doctoral Research Start-Up Fund of Hubei University of Science and Technology (Grant No. BK202316), Scientific Research Project of Hubei University of Science and Technology (Grant No. 2020-22GP08 and 2024-2025X08), Excellent Discipline Cultivation Project by Jianghan University (Grant No. 2023XKZ007). The authors also thank Home for Researchers editorial team (www.home-for-researchers.com) for language editing service.

Appendix A. Supplementary data

Supplementary data to this article can be found online at https://doi.org/10.1016/j.arabjc.2024.105996.

References

Vanessa S. Antonin, Felipe M. Souza, Victor S. Pinheiro, João P. C. Moura, Aline B. Trench, Caio Machado Fernandes, Marcos R. V. Lanza, Mauro C. Santos, Electrocatalytic hydrogen peroxide generation using WO3 nanoparticle-decorated sodium niobate microcubes, J. Electroanal. Chem. 959 (2024) 118190.

Benke, A., Mehner, E., Rosenkranz, M., Dmitrieva, E., Leisegang, T., Stöcker, H., Pompe, W., Meyer, D.C., 2015. Pyroelectrically driven •OH generation by barium titanate and palladium nanoparticles. J. Phys. Chem. C 119 (32), 18278–18286.

Chen, P., Zhou, W., Zhang, H., Pan, Q., Zhang, X., Chu, B., 2019. Large Thermal–electrical response and rectifying conduction behavior in asymmetrically reduced ferroelectric ceramics. ACS Applied Electronic Materials 1 (4), 478–484.

Dai, B., Guo, J., Gao, C., Yin, H., Xie, Y., Lin, Z., 2023. Recent advances in efficient photocatalysis via modulation of electric and magnetic fields and reactive phase control. Adv. Mater. 35, 2370100.

Fuentes-Pérez, M., Sotelo-Lerma, M., Fuentes-Ríos, J.L., Morales-Espinoza, E.G., Serrano, M., Nicho, M.E., 2021. Synthesis and study of physicochemical properties of Fe_3O_4@$ZnFe_2O_4$ core/shell nanoparticles. J. Mater. Sci. Mater. Electron. 32, 16786–16799.

C. Goutham, K. V. Ashok Kumar, S. S. Kumar Raavi, C. Subrahmanyam, S. Asthana, Enhanced electrical and photocatalytic activities in $Na_{0.5}Bi_{0.5}TiO_3$ through structural modulation by using anatase and rutile phases of TiO_2, J. Materiomics, 8 (2022) 18–29.

Guo, R., Liu, M., Xing, Y., Bai, T., Zhao, C., Huang, H., Zhang, H., 2023. Piezoelectrically enhanced photocatalysis of $K_xNa_{1-x}NbO_3$ (KNN) microstructures for efficient water purification. Nanoscale 15, 6920–6933.

Hasan, S., Azhdar, B., 2023. $NiFe_2O_4$ and $ZnFe_2O_4$ nanoparticles synthesis by sol-gel auto-combustion for humidity sensor applications. J. Sol-Gel Sci. Technol. 105, 416–429.

Huang, Z., Luo, N., Zhang, C., Wang, F., 2022. Radical generation and fate control for photocatalytic biomass conversion. Nat. Rev. Chem. 6, 197–214.

Inyang, M., Dickenson, E., 2015. The potential role of biochar in the removal of organic and microbial contaminants from potable and reuse water: a review. Chemosphere 134, 232–240.

Jiang, L., Yang, P., Fan, Y., Zeng, S., Wang, Z., Pan, Z., He, Y., Xiong, J., Zhang, X., Hu, Y., Gu, H., Wang, X., Wang, J., 2021. Ultrahigh piezoelectric coefficients of Li-doped (K, Na)Nb_O3 nanorod arrays with manipulated O-T phase boundary: towards energy harvesting and self-powered human movement monitoring. Nano Energy 86, 106072.

Jung, J.H., Lee, M., Hong, J.I., Ding, Y., Chen, C.Y., Chou, L.J., Wang, Z.L., 2011. Lead-free $NaNbO_3$ nanowires for a high output piezoelectric nanogenerator. ACS Nano 5 (12), 10041–10046.

Khan, A., Danish, M., Alam, U., Zafar, S., Muneer, M., 2020. Facile synthesis of a Z-scheme $ZnIn_2S_4$/MoO_3 heterojunction with enhanced photocatalytic activity under visible light irradiation. ACS Omega 5, 8188–8199.

Li, J., Jiang, J., Cheng, Q., Cui, Z., Liu, X., Zuo, P., Zhuang, Q., 2022. Construction of a flexible 1D core-shell Al_2O_3@$NaNbO_3$ nanowire/poly(p-phenylene benzobisoxazole) nanocomposite with stable and enhanced dielectric properties in an ultra-wide temperature range. J. Mater. Chem. C 10, 716–725.

Li, X., Li, B., Li, R., Yao, Y., Fan, N., Qi, R., Xu, Z., Cui, W., Xu, H., Shan, L., Liu, X., Dong, L., 2023. Synthesis of an efficient paramagnetic $ZnFe_2O_4$ agent for NIR-I/II responsive photothermal performance. J. Alloy. Compd. 936, 168161.

Li, T., Liu, Z., Meng, Y., 2022. Two-dimensional ultra-thin nanosheets optimize the surface reaction dynamics and photo/pyrogenerated carrier transfer of $NaNbO_3$ for an efficient pyro-photo-electric catalytic system. Sustainable Energy Fuels 6, 4227.

Li, Q., Ouyang, Y., Li, H., Wang, L., Zeng, J., 2021. Photocatalytic conversion of methane: recent advancements and prospects. Angew. Chem. Int. Ed. 61 (2), e202108069.

Li, L., Salvador, P.A., Rohrer, G.S., 2014. Photocatalysts with internal electric fields. Nanoscale 6 (1), 24–42.

Li, X., Shi, C., Feng, Z., He, J., Zhang, R., Yang, Z., Pan, P., Li, H., Feng, D., Zheng, L., 2023. Construction of Si nanowires/$ZnFe_2O_4$/Ag photocatalysts with enhanced photocatalytic activity under visible light and magnetic field. J. Alloy. Compd. 946, 169467.

Li, C., Zhang, N., Gao, P., 2023. Lessons learned: how to report XPS data incorrectly about lead-halide perovskites. Mater. Chem. Front. 7 (18), 3797–3802.

Li, S., Zhao, Z., Zhao, J., Zhang, Z., Li, X., Zhang, J., 2020. Recent advances of ferro-, piezo-, and pyroelectric nanomaterials for catalytic applications. ACS Appl. Nano Mater. 3, 1063–1079.

Liu, W., Du, M., Wang, Y., Liu, Y., Kang, S., 2024. Pyroelectric photocatalysis: polarization mechanism insight, in situ characterizations and challenges. Chem. Eng. J. 485, 149627.

Liu, S., Liu, Z., Meng, Y., 2022. Doping regulates pyro-photo-electric catalysis to achieve efficient water splitting in $Ba_{1-x}Sr_xTiO_3$ through solar energy and thermal resources. New J. Chem. 46, 17292–17302.

Liu, Y., Zhang, M., Wang, Z., He, J., Zhang, J., Ye, S., Wang, X., Li, D., Yin, H., Zhu, Q., Jing, H., Weng, Y., Pan, F., Chen, R., Li, C., Fan, F., 2022. Bipolar charge collecting structure enables overall water splitting on ferroelectric photocatalysts. Nat. Commun. 13, 4245.

Luo, Z., Ye, X., Zhang, S., Xue, S., Yang, C., Hou, Y., Xing, W., Yu, R., Sun, J., Yu, Z., Wang, X., 2022. Unveiling the charge transfer dynamics steered by built-in electric fields in BiOBr photocatalysts. Nat. Commun. 13, 2230.

Mateo, D., Cerrillo, J.L., Durini, S., Gascon, J., 2021. Fundamentals and applications of photo-thermal catalysis. Chem. Soc. Rev. 50, 2173–2210.

Modak, B., Modak, P., Ghosh, S.K., 2016. Improving visible light photocatalytic activity of $NaNbO_3$: a DFT based investigation. RSC Adv. 6, 90188–90196.

Naseer, H., Soomro, S.A., Gul, I.H., 2022. Increased dielectric properties of $ZnFe_2O_4$/rGO nanohybrid via thermo-chemical route. J. Aust. Ceram. Soc. 58, 1265–1274.

Ou, G., Li, Z., Li, D., Cheng, L., Liu, Z., Wu, H., 2016. Photothermal therapy by using titanium oxide nanoparticles. Nano Res. 9 (5), 1236–1243.

Qi, J.T., Swiatowska, J., Skeldon, P., Marcus, P., 2020. Chromium valence change in trivalent chromium conversion coatings on aluminium deposited under applied potentials. Corros. Sci. 167, 108482.

Qian, H., Liu, Z., Guo, Z., Ruan, M., Ma, J., 2020. Hexagonal phase/cubic phase homogeneous $ZnIn_2S_4$ n-n junction photoanode for efficient photoelectrochemical water splitting. J. Alloy. Compd. 830, 154639.

Qian, W., Wu, Z., Jia, Y., Hong, Y., Xu, X., You, H., Zheng, Y., Xia, Y., 2017. Thermo-electrochemical coupling for room temperature thermocatalysis in pyroelectric ZnO nanorods. Electrochem. Commun. 81, 124–127.

Qiao, Z., Liu, Z., Ruan, M., Guo, Z., Yan, W., Wu, X., 2021. Thermal excitation polarized field drives photoelectric catalysis for dye degradation in a $BaTiO_3$/CdS heterojunction through integration of solar and thermal energy. ChemPhotoChem. 5, 1106–1118.

Raufeisen, S., Stelter, M., Braeutigam, P., 2020. Pyrocatalysis—The DCF assay as a pH-robust tool to determine the oxidation capability of thermally excited pyroelectric powders. PLoS One 15, e0228644.

Soltani, T., Tayyebi, A., Lee, B.K., 2020. $BiFeO_3$/$BiVO_4$ p-n heterojunction for efficient and stable photocatalytic and photoelectrochemical water splitting under visible-light irradiation. Catal. Today 340, 188–196.

O. Sudhir Ekande, M. Kumar, Self-powered piezoelectric NaNbO3 induced band position rearrangement and electrocatalysis in MoS2/NaNbO3 heterojunction for generation of reactive oxygen species for organic pollutant removal, Chem. Eng. J. 458 (2023) 141454.

Sun, H., Cai, H., Li, L., Yang, Y., He, P., Zhou, K., Han, Y., Guan, J., Fan, X., 2021. Photothermal synergic catalytic degradation of the gaseous organic pollutant isopropanol in oxygen vacancies utilizing $ZnFe_2O_4$ and mechanism insight. J. Chem. Res. 45 (7–8), 773–780.

Sun, F., Xing, X.L., Zhang, C.Y., Zhang, J.R., Hong, H., 2024. Enhanced photocatalytic CO_2 reduction performance via photothermal-magnetic synergistic effects for solar fuel production. ACS Sustain. Chem. Eng. 12, 3298–3311.

Tian, S., Li, B., Dai, Y., Wang, Z.L., 2023. Piezo-phototronic and pyro-phototronic effects enhanced broadband photosensing. Mater. Today 68, 254–274.

Tu, S., Guo, Y., Zhang, Y., Hu, C., Zhang, T., Ma, T., Huang, H., 2020. Piezocatalysis and piezo-photocatalysis: catalysts classification and modification strategy, reaction mechanism, and practical application. Adv. Funct. Mater. 30, 2005158.

Wang, C., Tian, N., Ma, T., Zhang, Y., Huang, H., 2020. Pyroelectric catalysis. Nano Energy 78, 105371.

Wang, M., Wang, B., Huang, F., Lin, Z., 2019. Enabling piezopotential in piezoelectric semiconductors for enhanced catalytic activities. Angew. Chem. Int. Ed. 58, 7526–7536.

Wang, Y., Wang, S., Meng, Y., Liu, Z., Li, D., Bai, Y., Yuan, G., Wang, Y., Zhang, X., Li, X., Deng, X., 2022. Pyro-catalysis for tooth whitening via oral temperature fluctuation. Nat. Commun. 13, 4419.

Wang, K., Yang, P., Guo, R., Yao, X., Yang, W., 2019. Photothermal performance of MFe_2O_4 nanoparticles. Chin. Chem. Lett. 30, 2013–2016.

Wu, J., Mao, W., Wu, Z., Xu, X., You, H., Xue, A., Jia, Y., 2016. Strong pyro-catalysis of pyroelectric $BiFeO_3$ nanoparticles under a room-temperature cold–hot alternation. Nanoscale 8, 7343–7350.

Wu, Y., Wang, H., Tu, W., Wu, S., Chew, J.W., 2019. Effects of composition faults in ternary metal chalcogenides ($ZnIn_2S_{3+x}$, x = 1–5) layered crystals for visible-light-driven catalytic hydrogen generation and carbon dioxide reduction. Appl. Catal. b: Environ. 256, 117810.

Wu, S., Yan, T., Kuai, Z., Pan, W., 2020. Thermal conductivity enhancement on phase change materials for thermal energy storage: a review. Energy Storage Mater. 25, 251–295.

Xiao, F.X., Miao, J., Tao, H.B., Hung, S.F., Wang, H.Y., Yang, H.B., Chen, J., Chen, R., Liu, B., 2015. One-dimensional hybrid nanostructures for heterogeneous photocatalysis and photoelectrocatalysis. Small 11, 2115–2131.

Xu, W., Tian, W., Meng, L., Cao, F., Li, L., 2021. Interfacial chemical bond-modulated Z-scheme charge transfer for efficient photoelectrochemical water splitting. Adv. Energy Mater. 11, 2003500.

Xu, Y., Zhu, X., Yan, H., Wang, P., Song, M., Ma, C., Chen, Z., Chu, J., Liu, X., Lu, Z., 2022. Hydrochloric acid-mediated synthesis of $ZnFe_2O_4$ small particle decorated one-dimensional Perylene Diimide S-scheme heterojunction with excellent photocatalytic ability. Chin. J. Catal. 43, 1111–1122.

Yamazoe, S., Shibata, K., Kato, K., Wada, T., 2013. Needle-like $NaNbO_3$ synthesis via $Nb_6O_{19}^{8-}$ cluster using Na_3NbO_4 precursor by dissolution precipitation method. Chem. Lett. 42, 380–382.

Yang, Y., Wang, S., Zhang, Y., Wang, Z.L., 2012. Pyroelectric nanogenerators for driving wireless sensors. Nano Lett. 12, 6408–6413.

Yang, Y., Guo, W., Pradel, K.C., Zhu, G., Zhou, Y., Zhang, Y., Hu, Y., Lin, L., Wang, Z.L., 2012. Pyroelectric nanogenerators for harvesting thermoelectric energy. Nano Lett. 12, 2833–2838.

Yang, L., Xiang, Y., Jia, F., Xia, L., Gao, C., Wu, X., Peng, L., Liu, J., Song, S., 2021. Photo-thermal synergy for boosting photo-Fenton activity with rGO-$ZnFe_2O_4$: Novel photo-activation process and mechanism toward environment remediation. Appl. Catal. b: Environ. 292, 120198.

You, H., Ma, X., Wu, Z., Fei, L., Chen, X., Yang, J., Liu, Y., Jia, Y., Li, H., Wang, F., Huang, H., 2018. Piezoelectrically/pyroelectrically-driven vibration/cold-hot energy harvesting for mechano-/pyro-bi-catalytic dye decomposition of $NaNbO_3$ nanofibers. Nano Energy 52, 351–359.

You, H., Wu, Z., Wang, L., Jia, Y., Li, S., Zou, J., 2018. Highly efficient pyrocatalysis of pyroelectric $NaNbO_3$ shape-controllable nanoparticles for room-temperature dye decomposition. Chemosphere 199, 531–537.

You, H., Li, S., Fan, Y., Guo, X., Lin, Z., Ding, R., Cheng, X., Zhang, H., Lo, T.W.B., Hao, J., Zhu, Y., Tam, H.Y., Lei, D., Lam, C.H., Huang, H., 2022. Accelerated pyro-catalytic hydrogen production enabled by plasmonic local heating of Au on pyroelectric $BaTiO_3$ nanoparticles. Nat. Commun. 13, 6144.

Yu, H., Chen, F., Li, X., Huang, H., Zhang, Q., Su, S., Wang, K., Mao, E., Mei, B., Mul, G., Ma, T., Zhang, Y., 2021. Synergy of ferroelectric polarization and oxygen vacancy to promote CO_2 photoreduction. Nat. Commun. 12, 4594.

Yu, A., Qian, J., Liu, L., Pan, H., Zhou, X., 2012. Surface sprouting growth of $Na_2Nb_2O_6{\cdot}H_2O$ nanowires and fabrication of $NaNbO_3$ nanostructures with controlled morphologies. Appl. Surf. Sci. 258, 3490–3496.

Zhang, K., Cao, H., Dar, A., Li, D., Zhou, L., Wang, C., 2023. Construction of oxygen defective ZnO/$ZnFe_2O_4$ yolk-shell composite with photothermal effect for tetracycline degradation: Performance. Chin. Chem. Lett. 34, 107308.

Zhang, J., Gu, H., Wang, X., Zhang, H., Li, L., Wang, X., Dai, W.L., 2022. Facile and robust construction of a 3D-hierarchical $NaNbO_3$-nanorod/$ZnIn_2S_4$ heterojunction towards ultra-high photocatalytic H_2 production. Cat. Sci. Technol. 12, 2346–2359.

Zhang, Y., Kumar, S., Marken, F., Krasny, M., Roake, E., Eslava, S., Dunn, S., Da Como, E., Bowen, C.R., 2019. Pyro-electrolytic water splitting for hydrogen generation. Nano Energy 58, 183–191.

Zhang, Y., Su, H., Li, H., Xie, Z., Zhang, Y., Zhou, Y., Yang, L., Lu, H., Yuan, G., Zheng, H., 2021. Enhanced photovoltaic-pyroelectric coupled effect of $BiFeO_3$/Au/ZnO heterostructures. Nano Energy 85, 105968.

Zhang, L., Wang, K., Jia, Y., Fang, L., Han, C., Li, J., Shao, Z., Li, X., Qiu, J., Liu, S., 2022. Self-assembled $LaFeO_3$/$ZnFe_2O_4$/La_2O_3 ultracompact hybrids with enhanced piezo-phototronic effect for oxygen activation in ambient conditions. Adv. Funct. Mater. 32, 2205121.

Zhang, D., Wu, H., Bowen, C.R., Yang, Y., 2021. Recent advances in pyroelectric materials and applications. Small 17, 2103960.

Zhang, S., Zhang, B., Chen, D., Guo, Z., Ruan, M., Liu, Z., 2021. Promising pyro-photo-electric catalysis in $NaNbO_3$ via integrating solar and cold-hot alternation energy in pyroelectric-assisted photoelectrochemical system. Nano Energy 79, 105485.

Zhao, X., Liu, M., Wang, Y., Xiong, Y., Yang, P., Qin, J., Xiong, X., Lei, Y., 2022. Designing a built-in electric field for efficient energy electrocatalysis. ACS Nano 16, 19959–19979.

Zhao, C., Zhang, Y., Jiang, H., Chen, J., Liu, Y., Liang, Q., Zhou, M., Li, Z., Zhou, Y., 2019. Combined effects of octahedron NH_2-UiO-66 and flowerlike $ZnIn_2S_4$ microspheres for photocatalytic dye degradation and hydrogen evolution under visible light. J. Phys. Chem. C 123, 18037–18049.

Zhu, J., Xu, J., Du, X., Li, Q., Fu, Y., Chen, M., 2020. Photochemical deposition of amorphous MoS_x on one-dimensional $NaNbO_3$–CdS heterojunction photocatalysts for highly efficient visible-light-driven hydrogen evolution. Dalton Trans. 49 (26), 8891–8900.

Zhu, H.Y., Zheng, Z.F., Gao, X.P., Huang, Y.N., Yan, Z.M., Zou, J., Yin, H.M., Zou, Q.D., Kable, S.H., Zhao, J.C., Xi, Y.F., Martens, W.N., Frost, R.L., 2006. Structural evolution in a hydrothermal reaction between Nb_2O_5 and NaOH solution: from Nb_2O_5 grains to microporous $Na_2Nb_2O_6{\cdot}2/3H_2O$ fibers and $NaNbO_3$ cubes. J. Am. Chem. Soc. 128, 2373–2384.